Journal of Building Engineering 123 (2026) 115850

Contents lists available at ScienceDirect

Journal of Building Engineering

journal homepage: www.elsevier.com/locate/jobe

Effect of chemical and physico-chemical activation on the properties of 3D printed concrete with a low-cement multicomponent binder

Evaldas Serelis [a], Vitoldas Vaitkevicius [a,*], Lidija Korat Bensa [b], Vesna Zalar Serjun [b], Maris Sinka [c], Diana Bajare [c], Audrius Grinys [a], Karolina Butkute [a]

[a] Faculty of Civil Engineering and Architecture, Kaunas University of Technology (KTU), 51367, Kaunas, Lithuania
[b] Slovenian National Building and Civil Engineering Institute (ZAG), Department of Materials, Dimičeva ulica 12, 1000, Ljubljana, Slovenia
[c] Institute of Sustainable Building Materials and Engineering Systems, Riga Technical University (RTU), LV-1048, Riga, Latvia

ARTICLE INFO

Keywords:
3D concrete printing
Low-cement multicomponent binder
Chemical activation
Physico-chemical activation
Shrinkage

ABSTRACT

This research proposes an alternative low-cement multicomponent binder for extrusion-based 3D concrete printing to reduce CO_2 emissions associated with high Portland cement content. Due to the extremely low Portland cement content (100 kg/m^3), the proposed mixture presents several limitations, making it unsuitable for 3D printing without additional activation. To overcome these limitations, chemical and physico-chemical activation methods were applied to promote rapid early-age structuration, partly associated with accelerated ettringite formation, thereby improving compliance with the printing process requirements. The results demonstrate that both activation methods positively affect Portland cement hydration and improve printing-related properties. The research focuses primarily on the hardened properties of 3D-printed concrete, showing that activation reduces macroscopic porosity and increases density and compressive strength. The applied activation methods also increase overall shrinkage compared to the non-activated low-cement mixture. However, the absolute shrinkage remains approximately 25–30 % lower than that of a conventional reference mortar with a high Portland cement content. The suitability of the components used in the multicomponent binder was evaluated through pozzolanic activity testing. In contrast, the effects of chemical and physico-chemical activation on binder phase composition were investigated by X-ray diffraction, and the hardened properties of concrete were assessed using X-ray computed tomography, mercury intrusion porosimetry, shrinkage measurements, density, and compressive strength testing. The results demonstrate that chemical and physico-chemical activation enables the effective use of low-cement multicomponent binders in extrusion-based 3D concrete printing, providing a more sustainable alternative to conventional high-cement mixtures.

* Corresponding author.
E-mail address: vitoldas.vaitkevicius@ktu.lt (V. Vaitkevicius).

https://doi.org/10.1016/j.jobe.2026.115850
Received 27 January 2026; Received in revised form 24 February 2026; Accepted 14 March 2026
Available online 17 March 2026

1. Introduction

3D printing, also known as rapid prototyping, is a manufacturing technique in which three-dimensional objects are produced layer by layer using computer-aided design models [1]. Over the past decade, this technology has undergone significant development in concrete construction, enabling the fabrication of elements with complex geometries and varying levels of structural complexity, including construction elements, load-bearing components, and even full-scale buildings [2,3]. Recent studies have further demonstrated the structural potential of 3D-printed cementitious systems through the development of composite beams and permanent formwork concepts integrating ECC materials, combining additive manufacturing with structural design optimisation [4]. This technological progress has introduced significant design freedom for architects, while simultaneously posing new challenges for structural engineers, technologists, and materials specialists. Despite its advantages, 3D concrete printing still faces a significant limitation: cement-based mixtures used in this technology typically contain very high amounts of Portland cement [5], raising concerns about both environmental performance and practical applicability, particularly regarding CO_2 emissions.

Conventional 3D concrete printing mixtures typically contain between 400 kg/m^3 and 600 kg/m^3 of Portland cement [2,3], and in some cases even higher amounts [6,7]. Such high cement contents are commonly used to ensure stable extrusion, rapid early-age strength development, sufficient interlayer bonding, and overall buildability, while also compensating for printing-related defects. Recent studies on 3D-printed ECC systems have further highlighted the importance of interfacial bond behaviour between printed layers and subsequently cast concrete elements, demonstrating that interlayer quality plays a critical role in the structural performance of composite systems [8]. However, excessive cement contents introduce several drawbacks. Drying shrinkage may increase significantly, leading to the formation of microcracks [9], while 28-day compressive strength values typically range from 60 to 80 MPa, exceeding the requirements of most 3D concrete printing applications [10]. Moreover, a significant fraction of Portland cement remains unhydrated and primarily serves as an inactive microfiller [11]. Although high cement contents can resolve many technological challenges in 3D concrete printing, such mixtures become economically inefficient and environmentally unjustified when excessive strength is not required.

A more rational approach for 3D concrete printing would therefore be to use significantly lower Portland cement content. In conventional structural concrete, EN 206 specifies a minimum Portland cement content of 230 kg/m^3 [12]. In contrast, printable concrete mixtures typically contain around 400 kg/m^3 of cement. However, partial replacement with supplementary cementitious materials exhibiting pozzolanic properties – such as metakaolin, oil shale ash, glass powder, silica fume, fly ash, or blast furnace slag – has been explored [13–15]. In addition, engineered cementitious composites (ECC) adapted for extrusion-based 3D printing have been investigated for workability, interlayer performance, and hardened properties, including systems incorporating recycled aggregates and fibres, further emphasising the importance of rheological control and microstructural optimisation in printable cementitious materials [16]. Nevertheless, reductions in cement content to around 230 kg/m^3 remain uncommon in 3D printable systems. Only a limited number of studies have investigated cement contents below this threshold [17–19], and only one reported case achieved a reduction to approximately 75 kg/m^3, resulting in compressive strength values up to 40 MPa through thermal curing [20]. However, these mixtures were not intended for extrusion-based 3D concrete printing.

Such systems are typically based on multicomponent binder concepts that incorporate several pozzolanic constituents while relying on very low Portland cement content. Even if adapted for 3D concrete printing, many technological measures and curing strategies commonly applied in conventional concretes would be difficult or impractical to implement. The most critical limitation of low-cement multicomponent systems is insufficient early-age strength development, combined with inadequate shape retention, buildability, interlayer bonding, and green strength. These deficiencies raise significant uncertainty regarding their suitability for extrusion-based 3D concrete printing, and without additional activation measures, such systems would most likely not be printable.

Activation methods in 3D concrete printing are primarily applied to ensure sufficient green strength, enabling continuous printing with minimal or no technological interruptions. Typically, activation is implemented within the printhead or in proximity to the nozzle. Activation strategies reported in the literature can be broadly classified into chemical, physical (thermal), and mechanical approaches. Chemical activation commonly involves the use of accelerators introduced through in-line mixing [21], aluminium sulfate-based accelerators sprayed onto printed layers [22], or rapid mixing techniques combining dry constituents with chemical accelerators immediately before extrusion [23,22]. Physical or thermal activation methods include microwave heating applied near the nozzle to accelerate hydration kinetics [24]. Mechanical activation approaches include viscosity-based strategies relying on low water-to-cement ratios combined with mechanical vibration [25], the incorporation of magnetically responsive particles to enhance interlayer bonding [26], and gypsum-based activation combined with ultrasonic dispersion to promote rapid ettringite formation [27]. Most of these approaches aim to enhance green strength through accelerated ettringite formation [11,28].

However, these activation strategies have primarily been developed and validated for conventional 3D concrete printing mixtures containing relatively high Portland cement contents. For multicomponent binder systems with Portland cement contents around 100 kg/m^3, it remains unclear whether similar benefits can be achieved. Furthermore, several studies have reported that activation techniques may not only reduce compressive strength but also significantly increase drying shrinkage [9,29], thereby increasing the risk of additional cracking. Although shrinkage-related cracking may be mitigated with shrinkage-reducing admixtures, internal curing agents [30], expansive agents [31], or fibres [32], incorporating these measures increases mixture complexity and introduces additional challenges for printable systems.

From the authors' perspective, the most rational strategy for applying low-cement multicomponent binders in 3D concrete printing is a staged approach to compressive strength development. In this approach, fresh-state strength is primarily associated with rapid ettringite formation and accelerated early-age structuration; early-age strength development is governed by Portland cement hydration, and later-age strength gain results from the combined contributions of residual cement hydration and pozzolanic reactions.

Nevertheless, it remains unclear how activation methods that intensify early-age hydration and promote intensive ettringite formation-potentially followed by phase transformations into monosulfate or other aluminate hydrates [33–35] – affect the microstructural development of hardened low-cement multicomponent systems and whether such activation may lead to unfavourable long-term performance. Recent studies have demonstrated the increasing use of integrated non-destructive techniques, such as X-ray computed tomography combined with ultrasonic methods, for detailed assessment of internal microstructure and defect distribution in 3D-printed cementitious materials [36].

The objective of this study is not to optimise the binder composition itself, but to evaluate the compatibility of chemical and physico-chemical activation strategies promoting intensive ettringite formation with low-cement multicomponent binders intended for 3D concrete printing. The study aims to identify which activation approach provides the most favourable balance between early-age performance, microstructural refinement, compressive strength development, and shrinkage behaviour. The suitability of the components used in the multicomponent binder was evaluated through pozzolanic activity testing. In contrast, the effects of chemical and physico-chemical activation on binder phase composition were investigated by X-ray diffraction. The hardened properties of concrete were assessed using X-ray computed tomography, mercury intrusion porosimetry, early-age and long-term shrinkage measurements, density determination, and compressive strength testing. For this purpose, three systems based on the same low-cement multicomponent binder were examined: a reference mixture without activation, a chemically activated system, and a physico-chemically activated system. Although similar activation concepts are widely applied in conventional 3D concrete printing mixtures with high Portland cement contents, their applicability to low-cement multicomponent systems containing only 100 kg/m^3 of Portland cement remains largely unexplored.

2. Materials

Cement. Portland cement CEM I 42.5 N was used in the research. Main properties: Blaine fineness 3490 cm^2/g, density 3150 kg/m^3, average particle size 39.91 μm, initial and final setting times 163 and 204 min, 2-day and 28-day compressive strengths 32.1 and 58.5 MPa, and Bogue phase composition of C_3S 64.1%, C_2S 6.8%, C_3A 8.2%, and C_4AF 9.1%. The oxide composition is presented in Table 1, and the particle-size distribution is shown in Figs. 1 and 2.

Waste glass powder. Waste glass powder obtained from municipal solid waste was used in the research. Main properties: particle density 2380 kg/m^3, and specific surface area varied from 2080 cm^2/g to 5705 cm^2/g. For the primary research, a powder with a specific surface area of 3251 cm2/g and an average particle size of 79.41 μm was used. The oxide composition is presented in Table 1, and the particle-size distribution is shown in Figs. 1 and 2.

Oil shale ash. Oil shale ash obtained from the Eesti Elektrijaam power plant was used in the research. The ash was collected from the fly-ash stream using electrostatic precipitators and bag filters. Main properties: particle density 2580 kg/m^3, specific surface area 4450 cm^2/g, and average particle size 30.46 μm. The oxide composition is presented in Table 1, and the particle-size distribution is shown in Figs. 1 and 2.

Silica fume. Silica fume, also known as micro silica, is a by-product of silicon or ferrosilicon alloy production and was used in the research. Main properties: particle density 2252 kg/m^3, specific surface area 18.75 m^2/g (BET method), and average particle size 4.36 μm. The oxide composition is presented in Table 1, and the particle-size distribution is shown in Figs. 1 and 2.

Gypsum. Gypsum (β-calcium sulfate hemihydrate) was used as an additive to promote early-age strength development. Main properties: specific surface area (Blaine) 5000 cm^2/g, specific density 2318 kg/m^3, and average particle size 34.42 μm. Chemical composition: CaO 38.2%, SO_3 50.1%, insoluble residue 4.2%, and loss on ignition 6.8%.

Sand. Natural sand with a particle size fraction of 0/2 mm was used in the research. Main properties: particle density 2680 kg/m^3, bulk density 1540 kg/m^3, void ratio 39.1%, fines content (<63 μm) 0.33%, and average particle size 668.29 μm. The particle-size distribution is shown in Figs. 1 and 2.

Superplasticizer. A polycarboxylate ether (PCE)-based superplasticiser (Sika® ViscoCrete® D-190, Sika Sverige AB, Sweden) was

Table 1
Chemical composition of Portland cement, waste glass powder, oil shale ash, and silica fume.

Chemical composition	Quantity, %			
	CEM I 42.5 N	Glass powder	Oil shale ash	Silica fume
SiO_2	19.19	72.76	28.62	93.44
TiO_2	0.28	0.04	0.38	0.00
Al_2O_3	4.99	1.67	10.49	0.45
Fe_2O_3	2.96	0.79	3.40	0.19
MnO	0.03	0.02	0.06	0.00
MgO	1.48	2.09	4.60	0.41
CaO	62.77	9.74	33.58	0.20
SO_3	2.66	0.10	7.52	0.00
Na_2O	0.28	12.56	0.44	0.12
K_2O	0.83	0.76	3.45	0.13
P_2O_5	0.09	0.02	0.14	0.00
$Na_2O_{eq.}$	0.83	13.06	2.71	0.21
Loss on ignition	3.60	1.00	0.88	0.60

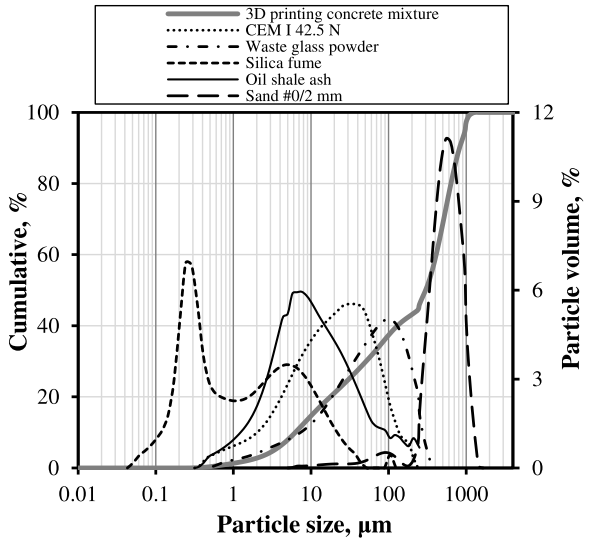

Fig. 1. Particle size distribution of Portland cement (CEM I 42.5 N), waste glass powder, oil shale ash, silica fume, 0/2 mm sand, and overall distribution of 3D printable concrete mixture.

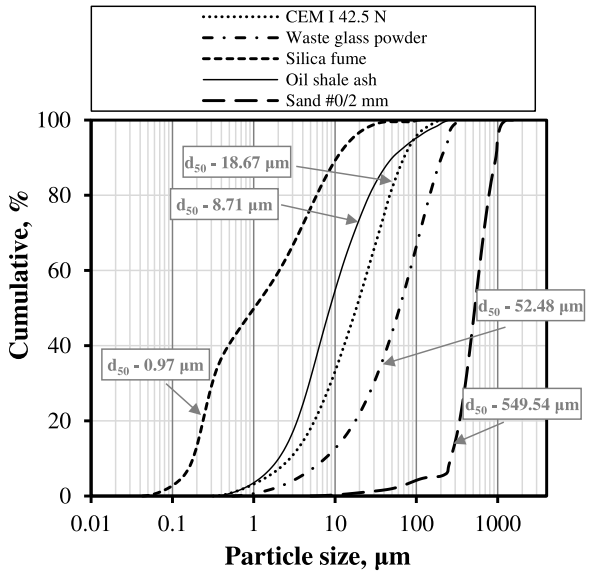

Fig. 2. Cumulative particle-size distribution of Portland cement (CEM I 42.5 N), waste glass powder, oil shale ash, silica fume, and 0/2 mm sand.

used to improve the workability of the mixtures. Main properties: brown liquid, specific gravity 1.08 ± 0.02 g/cm^3, pH 4.5 ± 1, and viscosity 128 ± 30 mPa s. The dosage was optimised based on preliminary tests to ensure adequate extrudability without segregation or bleeding.

Setting-regulating admixture. A calcium nitrate-based setting-regulating admixture (Sika® Frostschutz FS1, Sika Sverige AB, Sweden) was used to compensate for the retardation effects caused by waste glass powder and oil shale ash. The product contains approximately 58 wt—% $Ca(NO_3)_2$ (based on supplier information). The main properties are: density ~1.43 g/cm^3 and pH ~4.0. In the present study, the applied dosage (1.9 kg/m^3) corresponds to approximately 1.10 kg/m^3 of $Ca(NO_3)_2$ solids.

Accelerating admixture. An aluminium sulfate-based accelerating admixture (Sika® Sigunit® L-2655 AF, Sika Sverige AB, Sweden), commonly used in shotcrete technologies, was used in the research as a green-strength-gain additive. The main properties of the product are: liquid form, pH ~3, density ~1.51 g/cm^3, and dry matter content 51 ± 2.5 wt%. The product contains approximately 36 wt% aluminium sulfate (as supplied), which acts as a sulfate source in the system and was considered in the SO_3 input calculation. The product is alkali-free and chloride-free.

3. Methods

Mixture design. 3D-printed concrete mixtures were developed in accordance with paste film thickness and water film thickness principles, which state that a minimum paste volume is required to ensure sufficient lubrication and flowability while maintaining structural stability [37]. Accordingly, the Portland cement content was limited to 100 kg/m^3 to reduce CO_2 emissions and maximise the use of industrial waste materials.

The particle-size distribution of the mixture was designed using the modified Andreasen-Andersen packing model (q = 0.25), with d_{min} = 0.043 μm and D_{max} = 2000 μm. The combined particle-size distribution of the binder system (cement, waste glass powder, oil shale ash, and silica fume) and the 0/2 mm sand fraction was proportioned according to the target grading curve to obtain a dense binder-aggregate structure suitable for stable extrudability during multiple-layer deposition [38,39].

The binder system consisted of waste glass powder (WGP), oil shale ash (OSA), and silica fume (SF), each of which has been reported in the literature to provide specific and complementary benefits. OSA, due to its high CaO content, may increase pore-solution pH, thereby facilitating pozzolanic reactions and helping reduce shrinkage tendencies [40–42]. WGP, typically inert at early ages, may, however, enhance clinker dissolution and contribute to pozzolanic reactions at later stages [43–45]. SF, providing highly reactive silica, may act as a C–S–H nucleation aid and participate in pozzolanic reactions, thereby contributing to microstructural refinement [11,22,46]. A 0/2 mm sand fraction was used to improve overall printability and support smooth material flow during extrusion. A superplasticiser and a setting-regulating admixture were added to control water demand and mitigate the retardation effects commonly associated with WGP and OSA [11,40].

Four mixtures were prepared in this study (Table 2).

1) **3D concrete** – an unactivated printed 3D mixture.
2) **3D concrete + AS-ACC (chemical activation)** – a mixture activated using an aluminium sulfate-based accelerator, commonly used in shotcrete, to promote rapid early ettringite formation [18].
3) **3D concrete + G + HFUD (physico-chemical activation)** – a mixture activated using gypsum to support initial ettringite formation and to provide partial early strength from both ettringite and gypsum. In this mixture, a portion of waste glass powder was replaced with gypsum (by volume), based on the respective material densities, to maintain a comparable total binder volume and preserve the optimised particle packing distribution of the system, as determined by the modified Andreasen-Andersen model. This approach ensured direct comparability between mixtures without altering the optimised particle size distribution. Waste glass powder was selected as the substituted component because, compared to cement, oil shale ash, and silica fume, it has a relatively limited influence on early-age hydration kinetics and structural build-up, acting primarily as a fine filler within the multicomponent binder system. High-frequency ultrasonic dispersion (HFUD) was additionally applied to de-agglomerate particles, counteract gypsum-related retardation, and enhance early-age structuration and hydration kinetics [11,17,19,27].
4) **Reference mortar** – not intended for printing, but used as an additional mixture to compare shrinkage (early-age and long-term).

The overall mixture concept follows a staged strength development: early green strength from ettringite formation, early mechanical strength from cement hydration, and later-age strength from unreacted cement and from the pozzolanic reactions of WGP, OSA, and SF.

Mixing and activation procedure. All mixtures were prepared using a standardised 4-min mixing procedure (Table 3), including dry aggregate homogenization, incorporation of water and chemical admixtures, and final high-speed homogenization. After mixing, activation was applied depending on the mixture type.

1. **3D concrete** - no activation: prepared using the standardised mixing procedure, with no additional treatment applied.

Table 2
Mixture compositions used in the experimental program.

Component	Composition			
	3D concrete	3D concrete + AS-ACC	3D concrete + G + HFUD	Reference mortar
W/B	0.27	0.27	0.27	0.50
Water, kg/m^3	178.0	178.0	178.0	225
Portland cement, kg/m^3	100.0	100.0	100.0	450
Waste glass powder, kg/m^3	336.9	336.9	296.3	-
Oil shale ash, kg/m^3	163.1	163.1	163.1	-
Silica fume, kg/m^3	62.5	62.5	62.5	-
Gypsum, kg/m^3	-	-	39.5	-
Sand, kg/m^3	817.5	817.5	817.5	1350
Superplasticiser, kg/m^3	1.6	1.6	1.6	-
Setting-regulating admixture, kg/m^3	1.9	1.9	1.9	-
Accelerating admixture, kg/m^3	-	3.1	-	-
Total binder, kg/m^3	662.5	662.5	661.4	450.0
SO_3 input, kg/m^3	15.26	15.93	35.01	11.97

Table 3
Mixing procedure for 3D printable concrete.

Time, min	Mixing speed, rpm	Procedure
0-1	140	Dry component homogenization
1-2	140	Addition of full water content with chemical admixtures
2-3	140	Homogenization
3-4	285	Final homogenization

2. **3D concrete + AS-ACC (chemical activation)** - inline accelerator activation: prepared using the standardised mixing procedure; the aluminium-sulfate-based accelerator was introduced inline immediately before the printing nozzle, following common shotcrete practice.
3. **3D concrete + G + HFUD (physico-chemical activation)** - prepared using the standardised mixing procedure. Immediately after mixing, the fresh binder was ultrasonically treated for approximately 60 s using a high-frequency disperser (SONOPULS HD 3400, automatic resonance mode) at a set power of approximately 140 W. Under these conditions, the device operated within a stable power range around the selected value due to automatic resonance control. The treated batch volume was approximately 300 mL, corresponding to an average specific energy input of approximately 28 kJ/L. High-frequency ultrasonic dispersion (HFUD) was applied as a physico-chemical activation component, working in synergy with gypsum addition to enhance hydration kinetics and mixture homogeneity rather than acting as a stand-alone accelerator.
4. **Reference mortar** - no activation: mixed using the same procedure as the unactivated 3D-concrete mixture and used only for shrinkage comparison.

After preparation, all mixtures intended for printing were transferred to the printing feed system and extruded within 5 min.

3D printing process and curing. The printing process was carried out using a steel-frame gantry-type laboratory 3D printer (Fig. 3) with a printable area of 800 × 1200 × 800 mm, a 25 mm nozzle diameter, and a positioning accuracy of ±0.5 mm. The system used a screw-based continuous extrusion mechanism with a maximum printing speed of 100 mm/s. The pumping unit had a capacity of up to 12 L/min, a maximum operating pressure of 20 bar, a hopper volume of 68 L, a mixing motor power of 1.9 kW, and a maximum conveying distance and height of 30 m and 15 m, respectively. The printing process was controlled using Ultimaker Cura slicing software.

During specimen production, the average layer height was approximately 15 mm, and 5-6 layers were deposited, resulting in a total printed height of approximately 75-90 mm. The time interval between successive layers was typically within 60–120 s. Extrudability was assessed during printing and defined as the ability to achieve continuous and uniform material flow without nozzle blockage or

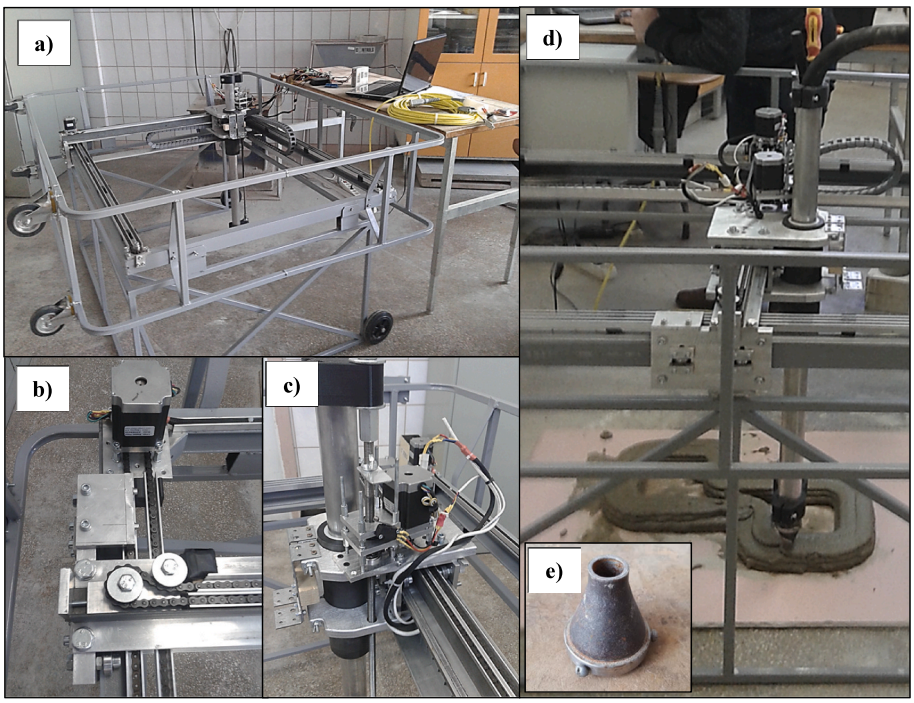

Fig. 3. The 3D concrete printer: a) stainless steel frame; b) X and Y axis chain drive system; c) Z axis vertical drive; d) 3D printing process; e) printing nozzle.

visible segregation. The open time was defined as the period during which the mixture remained extrudable and suitable for layer deposition. The non-activated mixture exhibited a comparatively long open time consistent with the initial setting time of the cement (~160 min) but showed limited early structural build-up. The activated mixtures demonstrated a reduced open time of approximately 18-22 min and improved shape stability during multi-layer deposition. Buildability was evaluated as the maximum stable printable height before visible lateral deformation, which was approximately 80 mm for the reference mixture. Interlayer bonding strength was not specifically investigated in the present study. Fresh mixture consistency was assessed using a Suttard viscometer, yielding 10 cm for the non-activated mixture and 6 cm for both activated mixtures. All printed specimens were cured under laboratory ambient conditions of 20 ± 2 °C and 40-60 % relative humidity.

Pozzolanic activity. The pozzolanic activity of the supplementary cementitious materials was assessed in accordance with the French standard NF P 18-513 (Annexe A) [46]. Waste glass powder was tested at different surface areas to evaluate the effect of fineness. At the same time, oil shale ash was analysed in two conditions - as received and after 72 h of controlled CO_2 exposure to eliminate the influence of free lime. Silica fume was tested in its supplied form. In each case, the amount of calcium hydroxide fixed by the material was determined using the standard procedure, and the resulting $Ca(OH)_2$ consumption was used as an indicator of pozzolanic reactivity.

X-ray diffraction (XRD) analysis. For XRD analysis, binder pastes were prepared using the same powder compositions as in Table 2, excluding sand. Three binder systems were analysed: the non-activated 3D binder, the binder activated with the aluminium-sulfate-based accelerator (3D binder + AS-ACC), and the binder activated with gypsum and high-frequency ultrasonic dispersion (3D binder + G + HFUD). All binders were cured under the same conditions as the corresponding 3D-printed mixtures until 28 days, after which hydration was stopped by grinding the material with isopropanol.

Mineralogical analysis was performed using a Panalytical Malvern Empyrean diffractometer equipped with a Cu-Kα radiation source (λ = 1.5406 Å). The powders (<63 μm) were dried at 60 °C and back-filled into 27 mm holders. Scans were collected over 5-45° 2θ with a 0.013° step and 150 s counting time at 45 kV and 40 mA. Phase identification was carried out using HighScore 4.8 with the PDF-4+ database, and quantitative analysis was performed via Rietveld refinement using both the external-standard and K-factor methods. NIST SRM 676a corundum was used as the external standard.

X-ray computed tomography (CT). Micro-CT was used to analyse the internal structure and pore architecture of 28-day 3D-printed specimens. Scanning was performed with an EasyTom XL Ultra 160–230 system (RX Solutions, France). Samples were cut from printed elements to dimensions of 45–55 × ~100 × 150–220 mm and mounted on a high-precision air-bearing rotation stage. A nanofocus X-ray source (100 kV, 73 μA) was used to acquire 1856 projections over 360° with a 16-bit flat-panel detector (2560 × 2048 pixels) at a voxel size of 60 μm. A 1 mm Al filter minimised beam hardening. The SOD and SDD were 199 mm and 412 mm, respectively. Reconstruction was performed using X-ACT software, and 3D segmentation and visualisation were carried out in Avizo (Thermo Fisher Scientific).

Mercury intrusion porosimetry (MIP). Pore volume, porosity, and pore size distribution of the 28-day 3D-printed mixtures were evaluated using an AutoPore IV 9500 porosimeter (Micromeritics) over a pressure range of 0.0033–206.8 MPa. Fragments were extracted from the mid-section of the printed specimens to match the CT regions of interest. Hydration was stopped by immersing the fragments in isopropanol, followed by drying at 40 °C for 24 h and sealed storage until testing. Pore size distribution was calculated using the Washburn equation with a mercury contact angle of 130° and a surface tension of 480 mN/m. Two measurements were performed per mixture, and the averaged results are reported.

Shrinkage measurement. Early-age (0–24 h) and long-term (1–90 days) drying shrinkage were measured on four mixtures listed in Table 1. Prism specimens (75 × 75 × 285 mm) were prepared, with three replicates per mixture. Fresh mortar was placed into moulds in two layers, each carefully compacted to ensure consolidation around the corners and gage studs. The top surface was levelled with a plexiglass trowel. To minimise restraint during the initial deformation, the front screw connecting the Orbit-type gage studs was released immediately after casting.

Shrinkage was recorded continuously using Orbit Swiss displacement transducers (range 5 mm; accuracy <0.1 μm; repeatability

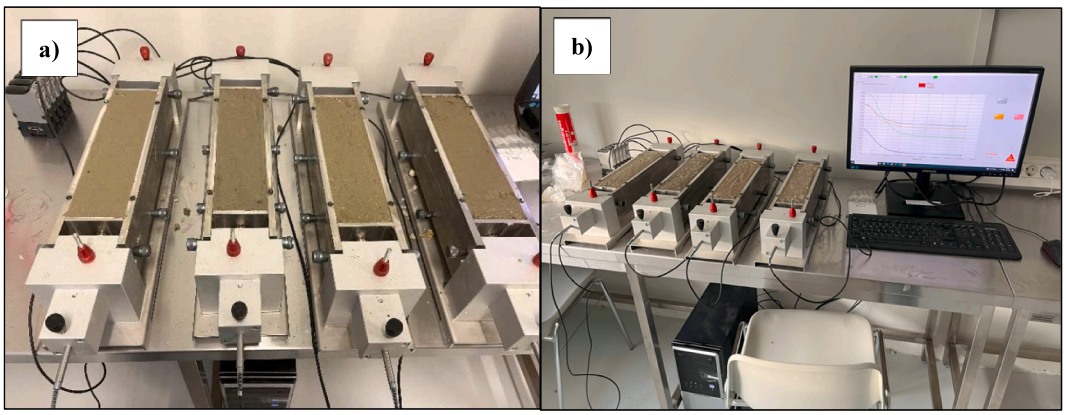

Fig. 4. Early-age and long-term drying shrinkage tests: (a) freshly poured mixes; (b) test setup.

<0.05 μm; resolution 0.01 μm) controlled via Sika Technology AG software. Measurements began immediately after compaction. To maintain curing conditions comparable to those of the 3D-printed elements, specimens were kept in laboratory air (20 ± 2 °C, 40–60 % RH). The top surface remained uncovered throughout the test. Specimens were demoulded after 24 h and monitored up to 90 days in the same environment. The test setup is shown in Fig. 4.

There is currently no standard for measuring early-age shrinkage (0–24 h), so this part of the procedure was based on approaches reported in recent studies, including Kurup et al. [30]. Long-term shrinkage (1–90 days) was measured under conditions similar to those used in common drying-shrinkage standards such as ASTM C157 [47] and ISO 1920-8 [48].

Compressive strength and density. Compressive strength was determined according to EN 12390-3 [49], and density according to EN 12390-7 [50]. 3D-printed samples were cut into prism specimens measuring approximately 40 × 40 × 160 mm. Density was determined after 1, 7, and 28 days. Compressive strength was tested at 60 min, 1 day, 7 days, and 28 days. Compressive strength and density results are presented as the average values calculated from six prisms.

4. Results

4.1. Pozzolanic reactivity

Pozzolanic reactivity of the selected materials (waste glass powder, oil shale ash, and silica fume) was evaluated using the lime consumption method in accordance with the French standard NF P18-513. Higher $Ca(OH)_2$ uptake indicates stronger pozzolanic reactivity. The main results of the pozzolanic reactivity assessment are presented in Fig. 5.

To determine an appropriate fineness of waste glass powder for application in a low-cement multicomponent binder, glass powders with different specific surface areas were analysed (Fig. 5). As the specific surface area increased from 2080 cm^2/g to 5705 cm^2/g, $Ca(OH)_2$ consumption increased from 430 mg to 618 mg. A practically rational $Ca(OH)_2$ consumption value of 597 mg was obtained at a specific surface area of 3251 cm^2/g. Although further grinding resulted in slightly higher pozzolanic reactivity, the improvement was insignificant compared with the rapidly increasing energy demand of the milling process. Therefore, waste glass powder with a specific surface area of 3251 cm^2/g was selected as the most rational option for further investigations of the low-cement multicomponent binder.

Considering that oil shale ash (OSA) contains a high CaO content (Table 1), its pozzolanic reactivity was evaluated using two approaches: in the as-received state and after 72 h of carbonation in a 5% CO_2 environment (Fig. 5). In the as-received state OSA exhibited a $Ca(OH)_2$ consumption of 560 mg per gram of material, whereas after the carbonation the $Ca(OH)_2$ uptake reduced to 173 mg, corresponding to an almost threefold decrease. This pronounced reduction is associated with a high free lime content in the as-received material. For further research, the uncarbonated oil shale ash was used. In comparison, silica fume exhibited the highest pozzolanic reactivity among the investigated materials (Fig. 5), consuming 1575 mg of $Ca(OH)_2$ per gram, approximately three times that of waste glass powder and oil shale ash.

It should be noted that the pozzolanic reactivity of waste glass powder, oil shale ash, and silica fume, as determined using the NF P18-513 method, represents a comparative assessment under controlled laboratory conditions, as the test is conducted at elevated temperature and in a highly water-saturated environment. Under practical curing conditions in cement-based systems, where both

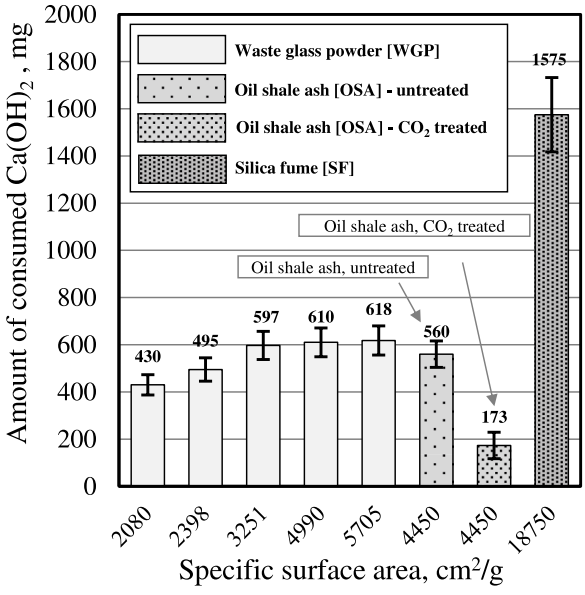

Fig. 5. Effect of specific surface area on the pozzolanic reactivity of waste glass powder, oil shale ash, and silica fume.

alkalinity and temperature are lower, the actual pozzolanic contribution of these materials is expected to be significantly reduced compared to values obtained using this method, and in low-cement multicomponent binder systems, may even remain limited or underdeveloped. Furthermore, both waste glass powder and oil shale ash exhibit complex chemical compositions, in which the presence of constituents such as Na_2O, K_2O, CaO, SO_3, etc., may influence not only the apparent pozzolanic reactivity but also the hydration process itself. Therefore, further microstructural analysis was carried out to support the interpretation of the low-cement multicomponent binder system under the applied activation methods.

4.2. XRD analysis

To evaluate the effect of the applied activation methods (chemical and physico-chemical) introduced at the fresh state on the phase composition of the low-cement multicomponent binder, both qualitative and quantitative XRD analyses were performed. The investigated systems included the reference 3D binder without activation, the chemically activated binder (3D binder + AS-ACC), and the physico-chemically activated binder (3D binder + G + HFUD). The analysis focused on the hardened binder state corresponding to 28 days of hydration. The main qualitative and quantitative XRD results are presented in Fig. 6 and Table 4.

The qualitative XRD patterns of the low-cement multicomponent binders when different activation methods were applied are presented in Fig. 6. In the reference 3D binder, unreacted clinker phases such as alite (C_3S, PDF 85-1378), belite (C_2S, PDF 20-0237), and tricalcium aluminate (C_3A, PDF 38-1429) were identified, while brownmillerite (C_4AF) was not detected. In addition, the main hydration products, including ettringite (AFt, PDF 41-1451) and portlandite (CH, PDF 04-0733), were observed. Secondary crystalline phases and filler-related components, such as calcite (PDF 05-0586), magnesite (PDF 08-0479), and quartz (PDF 46-1045), were also identified. Regardless of whether an activation method was applied or not, diffraction peaks of comparable intensity corresponding to ettringite and portlandite were detected in all investigated binders. Moreover, despite the very low Portland cement content, reflections associated with unreacted clinker phases remained clearly visible in all systems. A qualitative comparison of the XRD patterns revealed no substantial differences in the overall phase composition between the non-activated reference binder and the activated binders. A noticeable difference was observed only for the physico-chemically activated binder, where additional diffraction peaks attributable to gypsum (PDF 33-0311) were detected. To obtain more detailed information on the phase composition and relative phase contents of the investigated systems, the quantitative XRD results are discussed in the following section.

The results of the quantitative phase analysis performed using the Rietveld refinement method are presented in Table 4. To enable a direct comparison of the different activation methods, the phase composition of the hardened low-cement multicomponent binder was analysed with respect to individual phases and their relative changes under the different activation methods. In the reference 3D binder, 65.1 wt% of the amorphous phase was found. Upon chemical activation, the amorphous phase content decreased by approximately 0.5 wt%. In contrast, physico-chemical activation resulted in a decrease of roughly 1.0 wt%. The amorphous phase detected by quantitative XRD may include poorly crystalline hydration products and unreacted or partially reacted supplementary cementitious materials.

The content of unreacted clinker phases was evaluated based on the quantified amounts of alite (C_3S) and belite (C_2S). In the reference 3D binder, the total amount of unreacted clinker phases ($C_3S + C_2S$) was 19.2 wt%. Upon chemical activation, the total unreacted clinker content decreased to 18.1 wt%. A further reduction to 15.9 wt% was observed for the binder activated using physico-

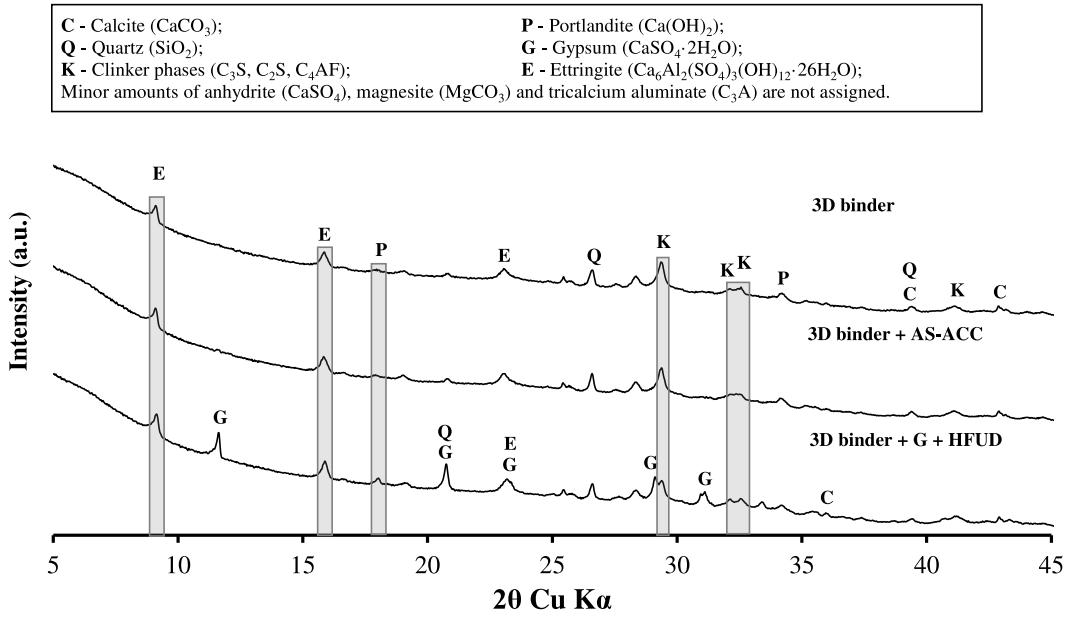

Fig. 6. XRD patterns of the 3D binder (W/B = 0.27) without activation, after chemical (AS-ACC) and physico-chemical (G + HFUD) activation.

Table 4
Quantitative phase composition of the 3D binder (W/B = 0.27) without activation, after chemical (AS-ACC) and physico-chemical (G + HFUD) activation.

Phase	3D binder, wt.%	3D binder + AS-ACC, wt.%	3D binder + G + HFUD, wt.%
Unreacted clinker			
$C_3S + C_2S$	19.2	18.1	15.9
C_3S	11.6	12.0	10.1
C_2S	7.6	6.1	5.8
C_3A	0.8	0.9	0.4
Main hydration products			
Ettringite	4.4	4.5	4.2
Portlandite	1.1	1.2	1.5
Secondary phases and fillers			
Gypsum	-	-	4.6
Calcite	7.3	8.1	7.4
Magnesite	1.0	0.8	0.7
Quartz	1.1	1.8	1.2
Amorphous (unclear phase — may include C-S-H and unreacted WGP, OSA, SF)			
Amorphous	65.1	64.6	64.1

chemical activation. Based on the quantified reduction in unreacted clinker phases, both activation methods led to a higher degree of Portland cement hydration than the reference binder.

The portlandite content in the reference 3D binder was 1.1 wt%. Upon chemical activation, the portlandite content increased slightly to 1.2 wt%. When physico-chemical activation was applied, a further increase to 1.5 wt% was observed. In contrast, the ettringite content remained at a similar level in all investigated binder systems and did not exhibit a systematic dependence on the applied activation method. No monosulfate or other aluminate hydrate phases were detected in any of the investigated binders. Minor variations were observed in the contents of calcite, magnesite, and quartz; however, their contribution to the overall phase composition remained insignificant. Overall, the quantitative XRD analysis did not reveal the formation of any additional crystalline phases attributable to the applied fresh-state activation methods in the hardened low-cement multicomponent binder.

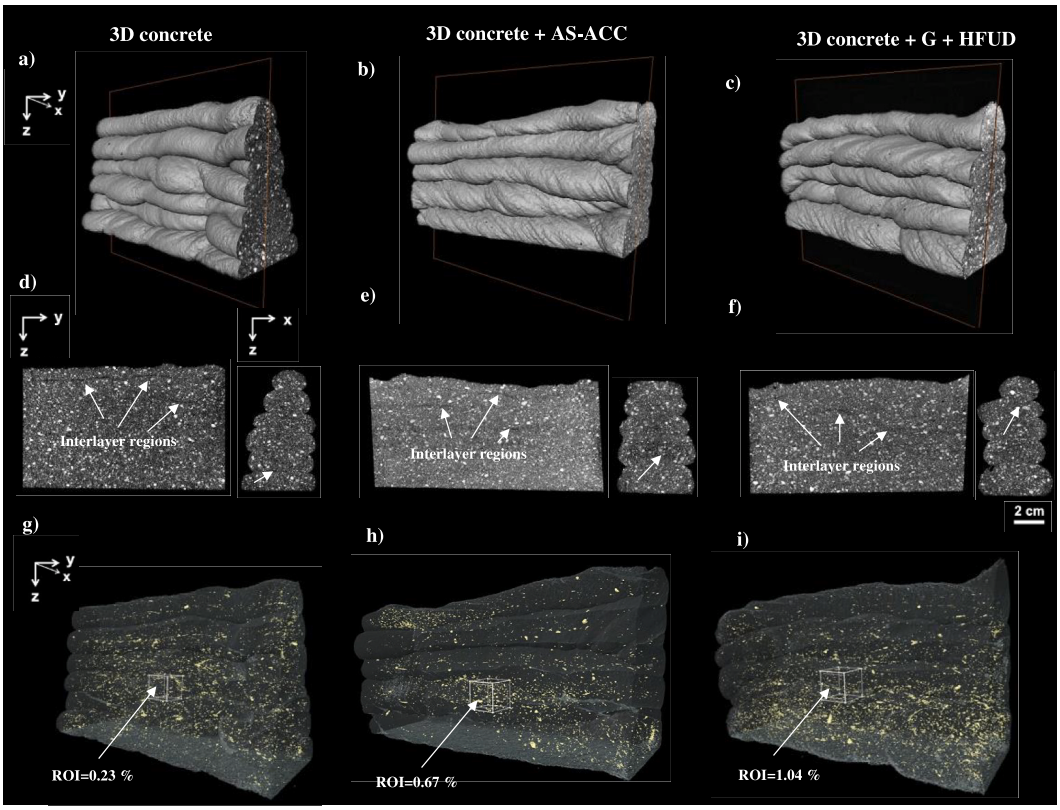

Fig. 7. X-ray computed tomography (CT) images of 3D-printed concrete mixtures under different activation methods: (a–c) extruded layer geometry; (d–f) interlayer regions; (g–i) CT-derived macropore visualisation and selected regions of interest (ROI) used for porosity quantification.

4.3. X-ray computed tomography analysis

X-ray computed tomography (CT) was used to analyse shape retention, interlayer regions, and CT-derived number-weighted pore-size distributions of 3D-printed concrete samples produced under three conditions: without activation (3D concrete), with chemical activation (AS-ACC), and with physico-chemical activation (G + HFUD). All 3D concrete mixtures were successfully printed to a comparable height (~8 cm), allowing direct comparison of their structural configuration. The main CT scan results are presented in Figs. 7 and 8.

In all cases, the printed layers exhibited relatively smooth surfaces, irrespective of the activation method, indicating stable extrusion without visible surface defects or filament disruption (Fig. 7a–c). The non-activated reference mixture (3D concrete) exhibited the poorest shape retention during printing, leading to a gradual deviation of the extruded layers from vertical alignment with increasing print height. In contrast, the chemically activated (AS-ACC) and physico-chemically activated (G + HFUD) mixtures maintained a more consistent layer geometry over the same printed height, with the chemically activated mixture exhibiting the most uniform geometry.

Longitudinal and cross-sectional CT sections revealed interlayer voids between printed layers in all mixtures, regardless of the applied activation method (Fig. 7d–f). These interlayer voids occurred as discontinuous, varying-length voids aligned with the printing direction. They were distributed throughout the printed height, observed in the lower, intermediate, and upper printed layers, without clear localisation. In the non-activated reference mixture (3D concrete), interlayer voids contained pores with diameters of approximately 150-200 μm. In the chemically activated mixture (AS-ACC), interlayer voids contained pores with diameters of approximately 200–250 μm. The physico-chemically activated mixture (G + HFUD) exhibited interlayer void diameters below 100 μm. Cross-sectional views further revealed apparent differences in shape retention and geometrical stability between the mixtures. The non-activated reference mixture (3D concrete) exhibited the poorest shape retention and geometrical stability during printing, resulting in noticeable deviations of layer alignment across the printed cross-section. In contrast, both activated mixtures exhibited improved layer alignment, with the chemically activated mixture (AS-ACC) showing the highest geometrical stability during printing.

Quantitative CT analysis was performed on selected regions of interest (ROI) representative of the extruded layers (Fig. 7g–i). The CT-detectable macroporosity measured in these regions was 0.23 % for the non-activated reference mixture, 0.67 % for chemical activation (AS-ACC), and 1.04 % for physico-chemical activation (G + HFUD), indicating an increased volume fraction of CT-resolvable macropores in the activated mixtures. These values represent only the fraction of macroporosity detectable by CT and should not be interpreted as total porosity.

The CT-derived number-weighted pore size distributions obtained from the selected regions of interest (Fig. 8) indicate that, in the equivalent pore diameter range of 150–300 μm, the occurrence of pores remained low and largely independent of the applied activation method. This suggests that, within this pore-size range, the overall printing-induced structural integrity and layer-deposition process were not negatively affected by either chemical or physico-chemical activation. In contrast, an evident influence of the activation methods was observed in the smaller CT-detectable pore size range of approximately 90–150 μm, where both chemical and physico-chemical activation resulted in a pronounced increase in the number of pores, with the most pronounced increase observed for the physico-chemically activated mixture. Pores within this size range have been reported in the literature to be associated with increased shrinkage-related deformations in cementitious materials. However, due to the limitations of CT analysis, further investigation is required to assess the influence of the applied activation methods on the microstructure. The implications of these microstructural features for the physical and mechanical properties of 3D-printed concrete are addressed in the following sections.

4.4. Mercury intrusion porosimetry analysis

Mercury intrusion porosimetry (MIP) analysis was applied to characterise the cumulative pore volume (Fig. 9) and the log differential intrusion pore size distribution (Fig. 10) of 3D-printed concrete under three conditions: without activation (reference 3D concrete), with chemical activation (AS-ACC), and with physico-chemical activation (G + HFUD). As shown in Fig. 9, the measurable pore diameter range for all investigated mixtures varied from approximately 0.006 μm to 383 μm. The total porosity measured by MIP in the reference mixture (3D concrete) was 33.6%. For the chemically activated mixture (AS-ACC), the total porosity determined by MIP remained similar to the reference mixture. In contrast, for the physico-chemically activated mixture (G + HFUD), the total

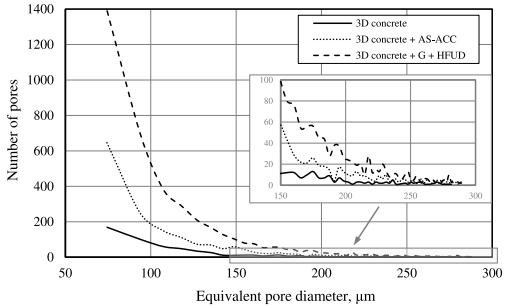

Fig. 8. CT-derived number-weighted pore size distributions for 3D-printed concrete mixtures under different activation methods.

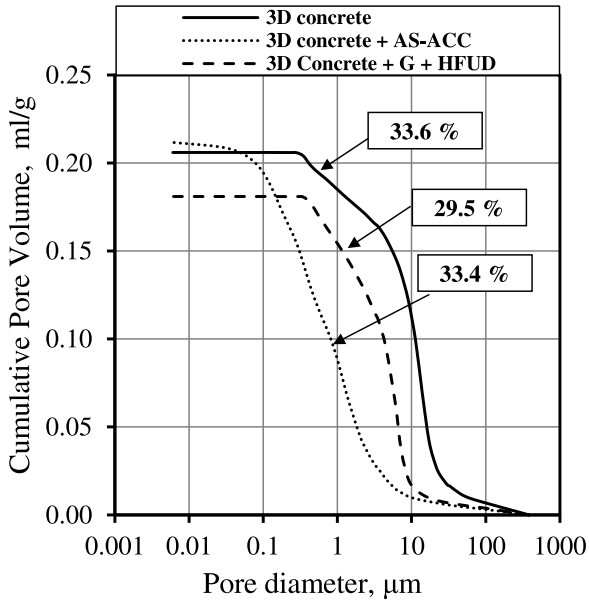

Fig. 9. Effect of activation methods on cumulative pore volume distribution.

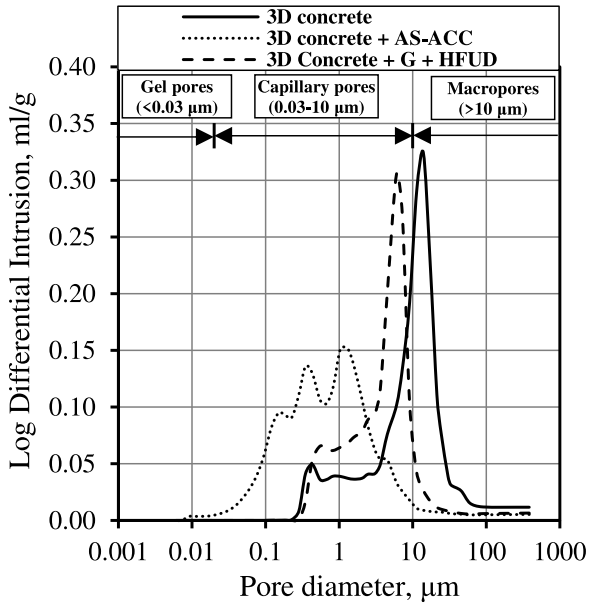

Fig. 10. Effect of activation methods on differential pore size distribution.

porosity determined by MIP decreased to 29.5%. In addition to changes in total porosity, both activation methods shifted the pore-size distribution toward smaller diameters.

The logarithmic differential intrusion pore size distributions are shown in Fig. 10. For clarity, the pore size ranges are grouped into gel pores (<0.03 μm), capillary pores (approximately 0.03–10 μm), and macropores (>10 μm). For the reference mixture (3D concrete), the log differential intrusion pore-size distribution showed dominant contributions in the capillary and macropore ranges, with two pronounced peaks at approximately 0.43 μm and 13.9 μm. For the physico-chemically activated mixture (G + HFUD), the overall shape of the log differential intrusion pore size distribution was similar to the reference mixture, although the pore size distribution shifted from the macropore range toward the capillary pore range. In this case, two distinct peaks were identified within the capillary pore range at approximately 0.7 μm and 6.0 μm, accompanied by a substantial reduction in macropores. By comparison, chemical activation (AS-ACC) resulted in a substantially altered log-differential intrusion pore-size distribution. In this case, the pore size distribution shifted almost entirely toward the capillary pore range, with only a minor contribution from macropores and three

pronounced peaks identified at approximately 0.22 μm, 0.35 μm, and 1.0 μm. Overall, both chemical activation (AS-ACC) and physico-chemical activation (G + HFUD) resulted in a reduction in macropores and an increase in the proportion of capillary pores. A decrease in macropores may improve compressive strength, whereas increased capillary porosity is mainly associated with increased shrinkage-related deformations.

4.5. Early-age and long-term shrinkage

To evaluate the influence of different activation methods on the shrinkage behaviour of 3D-printed concrete, deformations were measured during the early-age period (0-24 h) and the long-term period (1-90 days). In addition, the overall shrinkage was determined by combining the early-age and long-term deformations. The corresponding results are presented in Fig. 11. Four different compositions were analysed (Table 2): 3D concrete (without activation), 3D concrete + AS-ACC (chemically activated), 3D concrete + G + HFUD (physico-chemically activated), and a reference mortar, which was not intended for printing and was included solely for shrinkage comparison purposes.

During the first 24 h, the non-activated 3D concrete showed most of its early-age shrinkage within the first 12 h (−614 μm/m). In comparison, only a negligible deformation was observed between 12 and 24 h (−619 μm/m), as shown in Fig. 11a. When chemical activation was applied, the early-age shrinkage increased by approximately 33 %, from −619 μm/m (without activation) to −829 μm/m (with chemical activation). A further increase was observed for the physico-chemically activated mixture, where early-age shrinkage increased by approximately 44 %, from −619 μm/m (without activation) to −892 μm/m (with physico-chemical activation). By comparison, the reference mortar exhibited almost twice the early-age shrinkage as the 3D concrete, increasing from −619 μm/m (3D concrete) to −1264 μm/m (reference mortar). Although both chemical and physico-chemical activation increased early-age shrinkage, the deformations of the activated 3D concrete mixtures remained significantly lower than those of the reference mortar.

Over the period from 1 to 90 days, the long-term shrinkage of the 3D concrete (without activation) reached −143 μm/m (Fig. 11b). When physico-chemical activation was applied, the shrinkage increased by approximately 18 %, from −143 μm/m (without activation) to −169 μm/m (with physico-chemical activation). In contrast, chemical activation resulted in a more significant increase in long-term shrinkage, rising more than 2-fold from −143 μm/m (without activation) to −311 μm/m (with chemical activation). The reference mortar exhibited long-term shrinkage of approximately −250 μm/m, which is about 20 % lower than that of the chemically

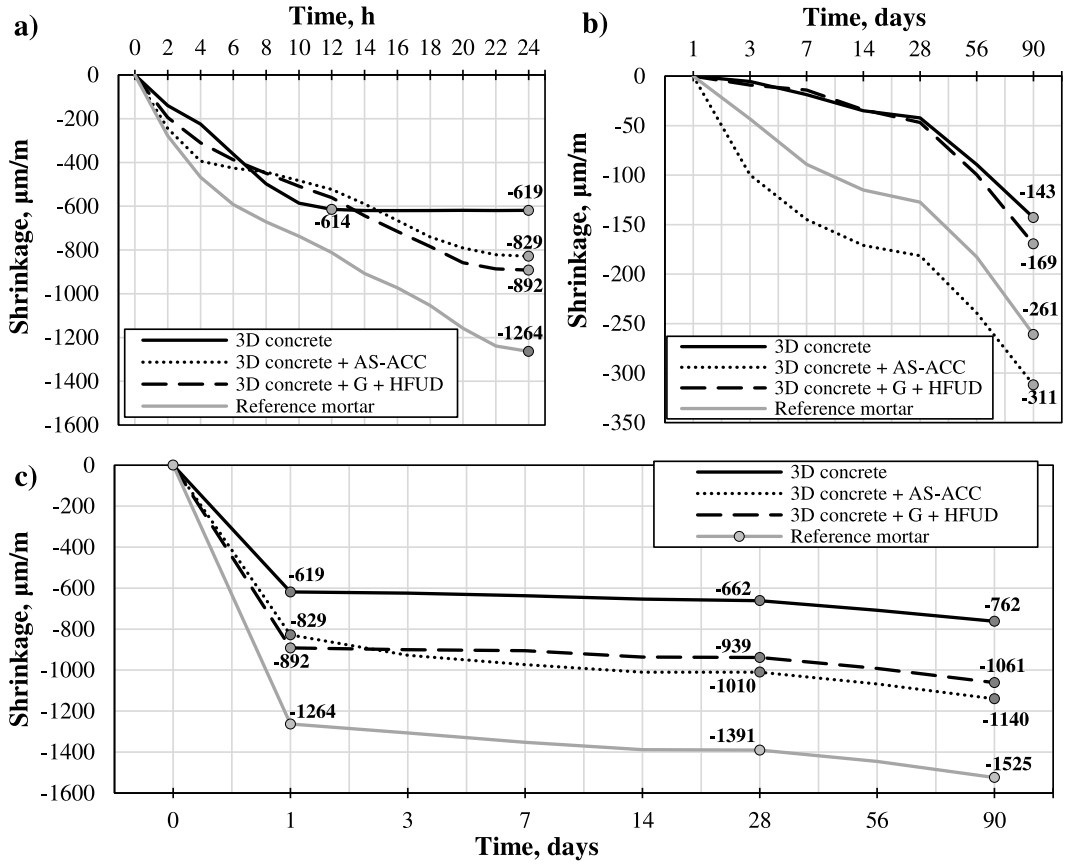

Fig. 11. Effect of activation methods on shrinkage behaviour of 3D-printed concrete: a) early-age shrinkage (0-24 h), b) long-term shrinkage (1-90 days), and c) overall shrinkage combining early-age and long-term deformation (0-90 days).

activated 3D concrete mixture.

Considering the combined effect of early-age and long-term deformations, the overall shrinkage of the 3D concrete (without activation) was −762 μm/m (Fig. 11c). When physico-chemical activation was applied, the overall shrinkage increased by approximately 39 %, from −762 μm/m (without activation) to −1061 μm/m (with physico-chemical activation). A further increase was observed for chemical activation, with overall shrinkage increasing by approximately 49%, from −762 μm/m (without activation) to −1140 μm/m (with chemical activation). The reference mortar exhibited an overall shrinkage of approximately −1525 μm/m, about twice that of the 3D concrete mixture. Regardless of the activation method, early-age shrinkage accounted for a significant portion of the overall deformation, contributing approximately 78-83% of the total shrinkage. Although the applied activation methods increased the overall shrinkage by 39–49 %, the resulting deformation values remained significantly lower (by approximately 25–30 %) compared to the reference mortar. It should be noted, however, that this reduction cannot be attributed solely to the reduced Portland cement content, as the low water-to-binder ratio (W/B = 0.27) required for 3D printing also plays a significant role in limiting drying shrinkage.

4.6. Density and compressive strength

The effects of the applied activation methods on the density and compressive strength of 3D-printed concrete are shown in Figs. 12 and 13. In the 3D concrete (without activation), the density measured after 1, 7, and 28 days was 1904, 1756, and 1754 kg/m^3, respectively. A slight decrease in density with increasing age may be due to the applied air-dry curing conditions. When chemical activation was applied (AS-ACC), the densities measured after 1, 7, and 28 days were 1985, 1841, and 1839 kg/m^3, respectively. For the physico-chemically activated mixture (G + HFUD), the corresponding density values were 2016, 1876 and 1873 kg/m^3 at 1, 7 and 28 days, respectively. Irrespective of the applied activation method, the density of the activated 3D-printed mixtures was approximately 80-120 kg/m^3 higher than that of the non-activated mixture (3D concrete).

Fig. 13 shows that green strength within the first 60 min after mixing was achieved only in the chemically and physico-chemically activated mixtures, with values of 0.38 MPa and 0.61 MPa, respectively. The compressive strength of the non-activated 3D concrete mixture was 1.5, 5.9, and 10.5 MPa at 1, 7, and 28 days, respectively. When chemically activated (AS-ACC), the compressive strength increased to 1.9, 7.3 and 11.6 MPa after 1, 7 and 28 days, respectively. Compared to the non-activated mixture, this corresponds to increases in compressive strength of approximately 27%, 33%, and 10% at the same ages. For the physico-chemically activated mixture (G + HFUD), the compressive strength increased to 2.1, 11.1 and 16.9 MPa after 1, 7 and 28 days, respectively. Compared to the non-activated mixture, this corresponds to increases in compressive strength of approximately 40%, 88%, and 61% at the same ages. Overall, both activation methods enabled early-age strength development within 60 min and led to higher compressive strength throughout the investigated curing period compared to the non-activated mixture (3D concrete).

5. Discussion

The primary practical significance of this research lies in demonstrating that extrusion-based 3D concrete printing can be achieved using a low-cement multicomponent binder containing only 100 kg/m^3 of Portland cement when chemical or physico-chemical activation is applied. One of the contributing factors enabling this was the accelerated formation and growth of ettringite crystals, which supported early structuration of the fresh mixture and contributed to the subsequent development of hardened properties.

The applied activation methods differed primarily in the mechanisms through which early-age strength was achieved. In the case of chemical activation, an aluminium sulfate-based accelerator induced rapid and intensive ettringite formation, resulting in very fast early structuration of the mixture. By contrast, physico-chemical activation relied on gypsum as the chemical activator, leading to less intensive ettringite formation, while part of the early strength was additionally influenced by gypsum hydration. The application of high-frequency ultrasonic dispersion provided a supplementary effect by deagglomerating particles and slightly increasing the mixture temperature, which further influenced hydration and hardening processes.

This early structuration, in which ettringite formation likely played an important role, enabled stable extrusion, sufficient shape retention, buildability, and relatively low interlayer porosity in the printed elements. Although slightly larger interlayer pores (approximately 200-250 μm) were observed in the chemically activated mixture compared to the physico-chemically activated system (<100 μm), these values were derived from selected interlayer regions of interest and therefore represent local characteristics rather than the global pore structure. Despite this, chemical activation generally provided slightly more stable printability and shape retention. Overall, both activation strategies proved effective in ensuring interlayer quality, but through different structuration mechanisms.

Both chemically and physico-chemically activated mixtures exhibited higher densities at all measured ages than the non-activated mixture. This suggests that activation resulted in a denser binder matrix, which may have limited the evaporation of excess water from the system. This observation is consistent with the MIP results, which showed slightly reduced total porosity in the activated mixtures. Improved water retention promoted greater cement hydration, as reflected by lower unreacted clinker phase content ($C_3S + C_2S$) and a slight increase in portlandite content. In the physico-chemically activated system, particle deagglomeration further enhanced hydration efficiency.

Although the low-cement multicomponent binder contains a high proportion of pozzolanic materials (waste glass powder, oil shale ash, and silica fume), their contribution under the applied curing conditions was limited. More favourable conditions, such as increased moisture availability, elevated temperature, or longer curing durations, would be required for pozzolanic reactions to become more effective. Such conditions were not investigated in this study.

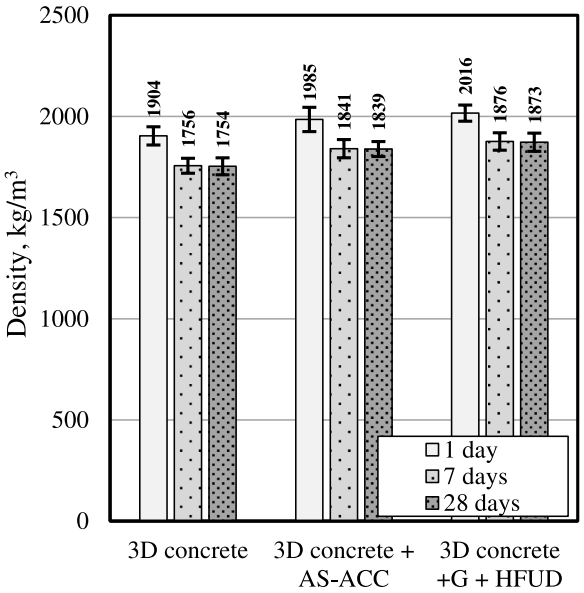

Fig. 12. Effect of activation methods on the density of 3D-printed concrete.

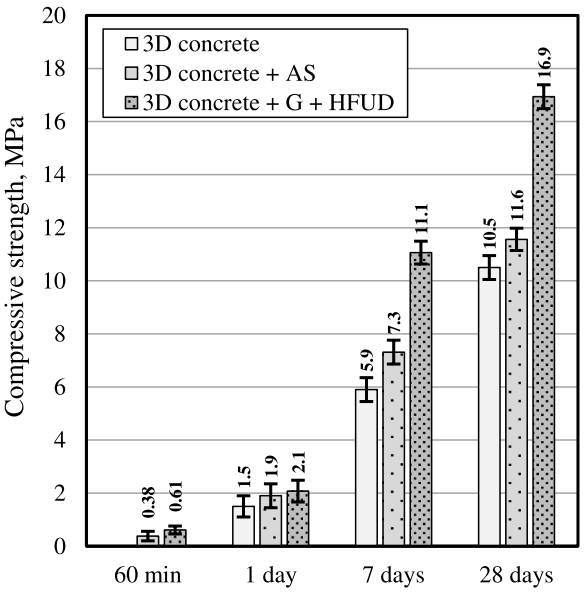

Fig. 13. Effect of activation methods on the compressive strength of 3D-printed concrete.

CT and MIP analyses revealed apparent differences in pore structure between the non-activated and activated mixtures. Activation did not increase macroporosity. Instead, it led to a redistribution of pores from the macropore range toward the capillary pore range. While macropore reduction is beneficial for strength development, an increased proportion of capillary pores is commonly associated with increased shrinkage deformations. Accordingly, both chemical and physico-chemical activation resulted in higher early-age, long-term, and overall shrinkage compared to the non-activated system. Nevertheless, although shrinkage increased with activation, the overall shrinkage of the low-cement multicomponent systems remained approximately 25–30% lower than that of the reference mortar. This reduction reflects the combined influence of reduced Portland cement content and the low water-to-binder ratio required for extrusion-based printing.

Both activation strategies had a clearly positive effect on density and compressive strength development compared to the non-activated mixture. The results indicate that chemical activation is more effective for rapid early structuration and printability, whereas physico-chemical activation offers advantages in pore structure refinement and later strength development. Several aspects related to long-term behaviour were not addressed in this research. In particular, the performance of binders that rely on intensive

early ettringite formation, as well as the presence of residual unreacted gypsum in the physico-chemically activated system, under prolonged moisture exposure or cyclic freezing and thawing conditions, remains unclear and should be addressed in future research. Furthermore, despite activation and the very low Portland cement content, a considerable fraction of unreacted clinker remained, indicating that the binder's hydration potential was not fully exploited. Due to the high overall binder content, shrinkage deformations may continue to develop under more favourable hydration conditions; therefore, the shrinkage values reported in this study should not be considered final.

6. Conclusions

Based on the investigation of a 3D-printed concrete mixture incorporating a low-cement multicomponent binder with constituents exhibiting pozzolanic potential and subjected to chemical and physico-chemical activation strategies, the following conclusions can be drawn.

1. XRD analysis indicated that physico-chemical activation enhanced cement hydration by reducing the amount of unreacted clinker phases compared to the non-activated system.
2. CT analysis showed that chemical activation provided the highest shape retention and printing stability of the printed layers, while physico-chemical activation resulted in the lowest interlayer pore sizes.
3. MIP analysis indicated that both activation methods reduced macroporosity in the hardened 3D-printed concrete, while chemical activation resulted in the most significant reduction of microporosity.
4. The applied activation methods led to an increase in both early-age and long-term shrinkage, while the overall shrinkage of the low-cement multicomponent binder system remained approximately 25-30 % lower compared to conventional high-cement reference mixtures.
5. Only the application of activation methods enabled the development of early-age (green) strength required for extrusion-based 3D concrete printing, and physico-chemical activation had the most potent effect on compressive strength development.

CRediT authorship contribution statement

Evaldas Serelis: Writing – original draft, Visualization, Supervision, Investigation, Funding acquisition, Conceptualization. **Vitoldas Vaitkevicius:** Supervision, Formal analysis. **Lidija Korat Bensa:** Writing – review & editing, Investigation. **Vesna Zalar Serjun:** Investigation. **Maris Sinka:** Project administration, Data curation. **Diana Bajare:** Supervision. **Audrius Grinys:** Investigation. **Karolina Butkute:** Supervision, Formal analysis.

Declaration of competing interest

The authors declare that they have no known competing financial interests or personal relationships that could have appeared to influence the work reported in this paper.

Acknowledgements

The authors acknowledge the financial support from:
- The Research Council of Lithuania (LMTLT), agreement No. S-M-ERA.NET-23-4, within the framework of the M-era.Net 3 project.
- The Slovenian Research and Innovation Agency: research core funding No. P2-0273 and Infrastructure programme No. I0-0032.
- The Latvian Council of Science project TRANSITION, agreement No. ES RTD/2023/24, supporting the contribution from Riga Technical University.

Data availability

Data will be made available on request.

References

[1] F. Bos, R. Wolfs, Z. Ahmed, T. Salet, Additive manufacturing of concrete in construction: potentials and challenges of 3D concrete printing, Virtual Phys. Prototyp. 11 (3) (2016) 209–225, https://doi.org/10.1080/17452759.2016.1209867.
[2] S.C. Paul, G.P. van Zijl, M.J. Tan, I. Gibson, A review of 3D concrete printing systems and materials properties: current status and future research prospects, Rapid Prototyp. J. 24 (4) (2018) 784–798, https://doi.org/10.1108/RPJ-09-2016-0154.
[3] Z. Zuo, Y. Zhang, J. Li, Y. Huang, L. Zhang, X. Wang, Y. Tao, W. De Corte, Systematic workflow for digital design and on-site 3D printing of large concrete structures: a case study of a full-size two-story building, J. Build. Eng. 104 (2025) 112370, https://doi.org/10.1016/j.jobe.2025.112370.
[4] M. Bai, J. Xiao, Y. Wu, T. Ding, Experimental and numerical study on the flexural behavior of 3D-printed composite beams with U-shaped ECC formwork, Eng. Struct. 312 (2024) 118225, https://doi.org/10.1016/j.engstruct.2024.118225.
[5] G.H. Ahmed, A review of "3D concrete printing": materials and process characterization, economic considerations and environmental sustainability, J. Build. Eng. 66 (2023) 105863, https://doi.org/10.1016/j.jobe.2023.105863.
[6] R. Wolfs, F. Bos, T. Salet, Hardened properties of 3D printed concrete: the influence of process parameters on interlayer adhesion, Cement Concr. Res. 119 (2019) 132–140, https://doi.org/10.1016/j.cemconres.2019.02.017.

[7] T.T. Le, S.A. Austin, S. Lim, et al., Mix design and fresh properties for high-performance printing concrete, Mater. Struct. 45 (2012) 1221–1232, https://doi.org/10.1617/s11527-012-9828-z.
[8] M. Bai, J. Xiao, T. Ding, K. Yu, Interfacial bond properties between 3D printed engineered cementitious composite (ECC) and post-cast concrete, Cement Concr. Compos. 157 (2025) 105897, https://doi.org/10.1016/j.cemconcomp.2024.105897.
[9] M.R. Shahmirzadi, A. Gholampour, A. Kashani, T.D. Ngo, Shrinkage behavior of cementitious 3D printing materials: effect of temperature and relative humidity, Cement Concr. Compos. 124 (2021) 104238, https://doi.org/10.1016/j.cemconcomp.2021.104238.
[10] T.A.M. Salet, Z.Y. Ahmed, F.P. Bos, H.L.M. Laagland, Design of a 3D printed concrete bridge by testing, Virtual Phys. Prototyp. 13 (3) (2018) 222–236, https://doi.org/10.1080/17452759.2018.1476064.
[11] D. Marchon, S. Kawashima, H. Bessaies-Bey, S. Mantellato, S. Ng, Hydration and rheology control of concrete for digital fabrication: potential admixtures and cement chemistry, Cement Concr. Res. 112 (2018) 96–110, https://doi.org/10.1016/j.cemconres.2018.05.014.
[12] EN 206:2013+A2, Concrete - Specification, Performance, Production and Conformity, 2021.
[13] M. Nodehi, T. Ozbakkaloglu, A. Gholampour, Effect of supplementary cementitious materials on properties of 3D printed conventional and alkali-activated concrete: a review, Autom. ConStruct. 138 (2022) 104215, https://doi.org/10.1016/j.autcon.2022.104215.
[14] S. Bhattacherjee, A.S. Basavaraj, A. Rahul, M. Santhanam, R. Gettu, B. Panda, E. Schlangen, Y. Chen, O. Copuroglu, G. Ma, L. Wang, M.A. Basit Beigh, V. Mechtcherine, Sustainable materials for 3D concrete printing, Cement Concr. Compos. 122 (2021) 104156, https://doi.org/10.1016/j.cemconcomp.2021.104156.
[15] Y. Chen, S. He, Y. Gan, O. Çopuroğlu, F. Veer, E. Schlangen, A review of printing strategies, sustainable cementitious materials and characterization methods in the context of extrusion-based 3D concrete printing, J. Build. Eng. 45 (2021) 103599, https://doi.org/10.1016/j.jobe.2021.103599.
[16] M. Bai, Y. Wu, J. Xiao, T. Ding, K. Yu, Workability and hardened properties of 3D printed engineered cementitious composites incorporating recycled sand and PE fibers, J. Build. Eng. 71 (2023) 106477, https://doi.org/10.1016/j.jobe.2023.106477.
[17] T. Proske, S. Hainer, M. Rezvani, C. Graubner, Eco-friendly concretes with reduced water and cement contents — mix design principles and laboratory tests, Cement Concr. Res. 51 (2013) 38–46, https://doi.org/10.1016/j.cemconres.2013.04.011.
[18] K. Robalo, H. Costa, R. Do Carmo, E. Júlio, Experimental development of low cement content and recycled construction and demolition waste aggregates concrete, Constr. Build. Mater. 273 (2021) 121680, https://doi.org/10.1016/j.conbuildmat.2020.121680.
[19] A. Alinejad, P. Sadeghian, A. Fam, Low-carbon gypsum-modified concrete with 80 % cement reduction and strength restoration by confinement, J. Build. Eng. 114 (2025) 114101, https://doi.org/10.1016/j.jobe.2025.114101.
[20] K. Robalo, E. Soldado, H. Costa, L. Carvalho, R. do Carmo, E. Júlio, Durability and time-dependent properties of low-cement concrete, Materials 13 (2020) 3583, https://doi.org/10.3390/ma13163583.
[21] Y. Tao, A. Rahul, K. Lesage, Y. Yuan, K. Van Tittelboom, G. De Schutter, Stiffening control of cement-based materials using accelerators in inline mixing processes: possibilities and challenges, Cement Concr. Compos. 119 (2021) 103972, https://doi.org/10.1016/j.cemconcomp.2021.103972.
[22] N. Zhang, J. Sanjayan, Pumping-less 3D concrete printing using quick nozzle mixing, Autom. ConStruct. 166 (2024) 105609, https://doi.org/10.1016/j.autcon.2024.105609.
[23] N. Zhang, J. Sanjayan, Surfactants to enable quick nozzle mixing in 3D concrete printing, Cement Concr. Compos. 142 (2023) 105226, https://doi.org/10.1016/j.cemconcomp.2023.105226.
[24] S. Muthukrishnan, S. Ramakrishnan, J. Sanjayan, Effect of microwave heating on interlayer bonding and buildability of geopolymer 3D concrete printing, Constr. Build. Mater. 265 (2020) 120786, https://doi.org/10.1016/j.conbuildmat.2020.120786.
[25] J. Sanjayan, R. Jayathilakage, P. Rajeev, Vibration induced active rheology control for 3D concrete printing, Cement Concr. Res. 140 (2021) 106293, https://doi.org/10.1016/j.cemconres.2020.106293.
[26] D. Jiao, C. Shi, G. De Schutter, Magneto-rheology control in 3D concrete printing: a rheological attempt, Mater. Lett. 309 (2022) 131374, https://doi.org/10.1016/j.matlet.2021.131374.
[27] V. Vaitkevičius, E. Šerelis, V. Kerševičius, Effect of ultra-sonic activation on early hydration process in 3D concrete printing technology, Constr. Build. Mater. 169 (2018) 354–363, https://doi.org/10.1016/j.conbuildmat.2018.03.007.
[28] V. Mechtcherine, F. Bos, A. Perrot, W.L. Da Silva, V. Nerella, S. Fataei, R. Wolfs, M. Sonebi, N. Roussel, Extrusion-based additive manufacturing with cement-based materials – production steps, processes, and their underlying physics: a review, Cement Concr. Res. 132 (2020) 106037, https://doi.org/10.1016/j.cemconres.2020.106037.
[29] A.P. Rubin, L.C. Quintanilha, W.L. Repette, Influence of structuration rate, with hydration accelerating admixture, on the physical and mechanical properties of concrete for 3D printing, Constr. Build. Mater. 363 (2023) 129826, https://doi.org/10.1016/j.conbuildmat.2022.129826.
[30] D.S. Kurup, M.K. Mohan, K. Van Tittelboom, G. De Schutter, M. Santhanam, A. Rahul, Early-age shrinkage assessment of cementitious materials: a critical review, Cement Concr. Compos. 145 (2023) 105343, https://doi.org/10.1016/j.cemconcomp.2023.105343.
[31] Z. Pan, Y. Zhu, D. Zhang, N. Chen, Y. Yang, X. Cai, Effect of expansive agents on the workability, crack resistance and durability of shrinkage-compensating concrete with low contents of fibers, Constr. Build. Mater. 259 (2020) 119768, https://doi.org/10.1016/j.conbuildmat.2020.119768.
[32] Y. Chen, L. Zhang, K. Wei, H. Gao, Z. Liu, Y. She, F. Chen, H. Gao, Q. Yu, Rheology control and shrinkage mitigation of 3D printed geopolymer concrete using nanocellulose and magnesium oxide, Constr. Build. Mater. 429 (2024) 136421, https://doi.org/10.1016/j.conbuildmat.2024.136421.
[33] B. Lothenbach, K. Scrivener, R. Hooton, Supplementary cementitious materials, Cement Concr. Res. 41 (12) (2011) 1244–1256, https://doi.org/10.1016/j.cemconres.2010.12.001.
[34] B. Lothenbach, F. Winnefeld, C. Alder, E. Wieland, P. Lunk, Effect of temperature on the pore solution, microstructure and hydration products of Portland cement pastes, Cement Concr. Res. 37 (4) (2007) 483–491, https://doi.org/10.1016/j.cemconres.2006.11.016.
[35] T. Matschei, B. Lothenbach, F. Glasser, The AFm phase in Portland cement, Cement Concr. Res. 37 (2) (2007) 118–130, https://doi.org/10.1016/j.cemconres.2006.10.010.
[36] M. Bai, J. Xiao, T. Ding, et al., Integrated non-destructive assessment of 3D printed UHPC microstructure using X-ray computed tomography and ultrasonic waves, Mater. Struct. 58 (2025) 258, https://doi.org/10.1617/s11527-025-02776-w.
[37] L.G. Li, A.K. Kwan, Concrete mix design based on water film thickness and paste film thickness, Cement Concr. Compos. 39 (2013) 33–42, https://doi.org/10.1016/j.cemconcomp.2013.03.021.
[38] K. Kondepudi, K.V. Subramaniam, B. Nematollahi, S.H. Bong, J. Sanjayan, Study of particle packing and paste rheology in alkali activated mixtures to meet the rheology demands of 3D concrete printing, Cement Concr. Compos. 131 (2022) 104581, https://doi.org/10.1016/j.cemconcomp.2022.104581.
[39] V. De Bono, N. Ducoulombier, R. Mesnil, J.F. Caron, Methodology for formulating low-carbon printable mortar through particles packing optimization, Cement Concr. Res. 176 (2024) 107403, https://doi.org/10.1016/j.cemconres.2023.107403.
[40] W. Salah Alaloul, M. Al Salaheen, A.B. Malkawi, K. Alzubi, A.M. Al-Sabaeei, M. Ali Musarat, Utilizing of oil shale ash as a construction material: a systematic review, Constr. Build. Mater. 299 (2021) 123844, https://doi.org/10.1016/j.conbuildmat.2021.123844.
[41] H. Tu, Z. Wei, A. Bahrami, N. Ben Kahla, A. Ahmad, Y.O. Özkılıç, Recent advancements and future trends in 3D concrete printing using waste materials, Dev. Built Environ. 16 (2023) 100187, https://doi.org/10.1016/j.dibe.2023.100187.
[42] J. Liiv, T. Teppand, E. Rikmann, T. Tenno, Novel ecosustainable peat and oil shale ash-based 3D-printable composite material, Sustain. Mater. Technol. 17 (2018) e00067, https://doi.org/10.1016/j.susmat.2018.e00067.
[43] A. Sivasuriyan, E. Koda, Incorporation of waste glass powder in the sustainable development of concrete, Materials 18 (2025) 3223, https://doi.org/10.3390/ma18143223.
[44] M. Bameri, M. Mohammadhasani, A. Khaloo, A. Ashour, M. NikKhah, Influence of waste glass powder as a supplementary cementitious material (SCM) on the mechanical properties, expansion, environmental impact, and microstructure of cementitious mortar, Eng. Rep. 7 (6) (2025) e70238, https://doi.org/10.1002/eng2.70238.

[45] H. Tao, J. Tang, C. Zhang, C. Zhou, W. Zhai, Synergistic utilization of recycle cement powder and glass powder to prepare low-carbon and environmentally friendly mortar: mechanical properties, microstructure, and environmental assessment, Mater. Today Sustain. 32 (2025) 101228, https://doi.org/10.1016/j.mtsust.2025.101228.
[46] Association Française de Normalisation (AFNOR), NF P18-513: Pozzolanic Addition for Concrete - Metakaolin - Definitions, Specifications and Conformity Criteria, AFNOR, 2012.
[47] ASTM C157/C157M-17, Standard Test Method for Length Change of Hardened Hydraulic-Cement Mortar and Concrete, ASTM International, West Conshohocken, PA, USA, 2024.
[48] ISO 1920-8, Testing of Concrete — Part 8: Determination of Drying Shrinkage of Concrete for Samples Prepared in the Field or in the Laboratory, International Organization for Standardization, Geneva, Switzerland, 2009.
[49] EN 12390-3, Testing Hardened Concrete - Part 3: Compressive Strength of Test Specimens, 2019.
[50] EN 12390-7, Testing Hardened Concrete - Part 7, Density of hardened concrete, 2019.